

behaves as a donor, which is not expected.

For the alkali-metal dopants K and Rb, the high-frequency modes show a BWF interference lineshape. As discussed above, this interference introduces a frequency renormalization for the high-frequency modes. Without a detailed analysis involving the spectral shape of the interfering continuum excitations, as we performed earlier for CsC₈ (ref. 10), we cannot separate the two contributions (that is, charge transfer and interference coupling (1/q)) to the phonon frequency ω₀ (equation (1)). Consequently, a quantitative statement about the charge-transfer-induced shift in the alkali-metal-doped SWNTs cannot be made at present. Although the one-dimensional nature of the SWNTs is expected to alter the nature of the continuum excitations, the T ≈ 300 K BWF frequency ω₀ of ~1,567 cm⁻¹ (Rb) and 1,565 cm⁻¹ (K) observed in the doped SWNT bundles is remarkably close to that in the stage 1 MC₈ GICs: 1,547 cm⁻¹ (KC₈) and 1,519 cm⁻¹ (CsC₈) for T ≈ 300 K. The coupling constants (1/q) are, however, a factor of ~3 higher in the GICs. We can say that the alkali-metal-doped SWNT Raman spectra qualitatively indicate that the bundles are highly doped, which is consistent with the large weight uptake (effective composition KC₈) observed by Lee *et al.*³.

We have also investigated the temperature stability in vacuum of the alkali-metal-doped SWNT bundles. A series of Raman spectra were taken on a Rb-doped SWNT sample as a function of temperature in the range 24–380 °C. The spectra were measured with the Rb-containing end of the evacuated ampoule at room temperature while the sample end of the ampoule was heated to progressively higher temperatures and equilibrated. A frequency decrease, probably associated with the thermal expansion of the SWNTs, and a broadening of the BWF peak, was observed at the highest temperatures. Interestingly, near ~200 °C, sharp Raman peaks around 1,480 and 1,590 cm⁻¹ were observed as shoulders on the BWF resonance, suggesting the existence of a metastable phase near 200 °C with a different structural arrangement for the Rb ions. At elevated temperatures, these additional peaks disappeared. At the highest temperature (380 °C), the Raman spectra suggests that the Rb remains bonded to the tube wall. *In situ* studies of Br₂ uptake at T ≈ 300 K in these SWNT bundles also reveal an intermediate-concentration phase. In this case, the high-frequency peak at 1,593 cm⁻¹ was found to quickly (<5 min) increase in frequency on exposure to bromine vapour and attain an intermediate value (1,603 cm⁻¹); after some time, the frequency changed rapidly to the saturation-doped value (1,617 cm⁻¹). □

Received 21 February; accepted 3 June 1997.

1. Thess, A. *et al.* Crystalline ropes of metallic carbon nanotubes. *Science* **273**, 483–487 (1996).
2. Dresselhaus, M. S., Dresselhaus, G. & Eklund, P. C. *Science of Fullerenes and Carbon Nanotubes* Ch. 19 (Academic, San Diego, 1996).
3. Lee, R. S., Kim, H. J., Fischer, J. E., Thess, A. & Smalley, R. E. Conductivity enhancement in single-walled carbon nanotube bundles doped with K and Br. *Nature* **388**, 255–257 (1997).
4. Dresselhaus, M. S. & Dresselhaus, G. Intercalation compounds of graphite. *Adv. Phys.* **30**, 139–326 (1981).
5. Ajayan, P. M. & Iijima, S. Capillarity-induced filling of carbon nanotubes. *Nature* **361**, 333–334 (1993).
6. Ajayan, P. M. *et al.* Opening carbon nanotubes with oxygen and implications for filling. *Nature* **362**, 522–525 (1993).
7. Rao, A. M. *et al.* Diameter-selective Raman scattering from vibrational modes in carbon nanotubes. *Science* **275**, 187–191 (1997).
8. Zhu, Q. *et al.* Intercalation of solid C₆₀ with iodine. *Nature* **355**, 712–714 (1992).
9. Kobayashi, M. *et al.* X-ray diffraction study of iodine-doped C₆₀. *Solid State Commun.* **81**, 93–95 (1992).
10. Eklund, P. C. & Subbaswamy, K. R. Analysis of Breit-Wigner line shapes in the Raman spectra of graphite intercalation compounds. *Phys. Rev. B* **20**, 5157–5161 (1979).
11. Zhou, P., Wang, K. A., Eklund, P. C., Dresselhaus, M. S. & Dresselhaus, G. Raman scattering study of the electron-phonon interaction in M₃C₆₀. *Phys. Rev. B* **48**, 8412–8417 (1993).
12. Eklund, P. C., Dresselhaus, G., Dresselhaus, M. S. & Fischer, J. E. Raman scattering from in-plane modes in low-stage graphite-alkali-metal compounds. *Phys. Rev. B* **16**, 3330–3333 (1977).
13. Eklund, P. C., Arakawa, E. T., Zarestky, J. L., Kamitakahara, W. A. & Mahan, G. D. Charge-transfer-induced changes in the electronic and lattice vibrational properties of acceptor-type GICs. *Synth. Metals* **12**, 97–102 (1985).

Acknowledgements. We thank L. Grigorian (Univ. Kentucky) for experimental assistance. We also thank K. R. Subbaswamy and E. Richter (Univ. Kentucky), and M. S. Dresselhaus and G. Dresselhaus (MIT), for discussions. This work was supported by the NSF and DDE.

Correspondence and requests for materials should be addressed to P.C.E. (e-mail: eklund@pop.uky.edu).

Seismological evidence for three-dimensional melt migration beneath the East Pacific Rise

Robert A. Dunn & Douglas R. Toomey

Department of Geological Sciences, University of Oregon, Eugene, Oregon 97403, USA

The extent to which crustal processes along mid-ocean ridges are controlled by either the pattern of mantle upwelling or the mode of magma injection into the crust is not known. Models of mantle upwelling vary from two-dimensional, passive flow¹ to three-dimensional, diapiric flow^{2–4}. Similarly, beneath a ridge segment bounded by tectonic offsets, crustal magma chambers may be replenished continuously along the ridge^{5–7} or at a central injection zone^{2–4} from which magma migrates towards the segment's ends. Here we present tomographic images that reveal the seismic structure and anisotropy of the uppermost mantle beneath the East Pacific Rise. The anisotropy is consistent with two-dimensional mantle flow diverging from the rise, whereas the anomalous isotropic structure requires a three-dimensional but continuous distribution of melt near the crust–mantle interface. Our results indicate that crustal magma chambers are replenished at closely spaced intervals along-axis and that crustal systems inherit characteristics of scale from melt transport processes originating in the mantle.

The site of our investigation lies midway along a 100-km-long section of the East Pacific Rise (EPR) bounded by the 9°03' N overlapping spreading centre and the Clipperton transform, a comparatively well studied section of oceanic ridge (Fig. 1). Its broad axial summit², axial-magma-chamber (AMC) reflector^{8,9}, crustal low seismic-wave velocity^{6,10}, and low-Q zone¹¹ are characteristic of a fast-spreading ridge that is magmatically robust. Apart from the overlapping spreading centre, the rise axis is continuous except for a series of fine-scale morphological discontinuities where the local trend of the rise changes abruptly by 10°–15° (refs 2, 5, 12). Such deviations from axial linearity ('devals') segment the rise at intervals of 10–20 km and show no off-axis trace^{2,5}. Devals are thought to demarcate axial hydrothermal systems¹², petrologically distinct lava^{5,13} and the axial continuity of the AMC reflector⁹. Crustal tomography^{6,11,14} reveals an axially varying seismic structure that also correlates with the segmentation observed in sea-floor morphology and geology. As comparatively little is known about the structure at sub-crustal depths, the origin of this segmentation is enigmatic. It may derive from magmatic processes occurring in the mantle or from tectonic and hydrothermal processes confined to the crustal carapace.

Our tomographic analysis includes delay times from 1,362 crustal and 200 P_n (mantle) refractions (Fig. 2a). Examination of Fig. 2b, which shows delay times for sets of receivers on opposing sides of the rise, suggests that the data are consistent with both seismic heterogeneity and anisotropy within the uppermost mantle. To permit imaging in anisotropic media, we modified our tomographic method¹⁴ to allow an azimuthally anisotropic upper mantle, a symmetry system in accord with previous studies of oceanic P_n arrivals (see review in ref. 15). The velocity of P_n waves for this symmetry system follows a cos(2θ) relationship, where θ is the azimuth of energy propagation¹⁵. We define a slowness model (slowness is the inverse of velocity) as

$$u'(r, \theta_p; u(r), a(r), \theta(r)) = \frac{u(r)}{1 + \frac{a(r)}{2} \cos[2(\theta(r) - \theta_p)]} \quad (1)$$

where $u(\mathbf{r})$ is the average slowness at nodal position \mathbf{r} , $a(\mathbf{r})$ is the percentage anisotropy defined as $(v_{\max} - v_{\min})/v_{\text{average}}$, where v is P-wave velocity, $\theta(\mathbf{r})$ is the azimuth of the fast direction for P waves, and θ_p is the azimuth of energy propagation. With the exception that the slowness model is defined by equation (1), we follow a previous implementation of the shortest-path technique¹⁴ to calculate ray paths and travel times through three-dimensional models that explicitly include sea-floor relief. The inverse problem is regularized by minimizing a stochastic penalty function and model roughness. Prior uncertainties in model parameters were 10% in $u(\mathbf{r})$, 10% in $a(\mathbf{r})$ and 8° in $\theta(\mathbf{r})$, and the decay length of the roughness operator was set at 125% of the interval between

perturbational nodes (see ref. 14 for details). From a one-dimensional starting model¹⁰, tomographic inversions first calculated the best-fitting two-dimensional (axially invariant) model and then used this result to find the best fitting three-dimensional model. All inversions included several iterations of the forward and inverse problems to incorporate ray-bending effects.

The results of several tomographic analyses are presented in Fig. 3a–d. Images are shown for three inversions where the percentage of anisotropy was fixed at 0%, 6% and 12%, and the tomographic analyses determined the azimuth of anisotropy and perturbations to the isotropic component of velocity (Fig. 3a–c). Figure 3d shows the results for an inversion where all parameters, including percentage

Figure 1 Sea-floor bathymetry and geometry of the seismic tomography experiment. Bathymetry is contoured at 100-m intervals, grey shade changes every 200 m; the 2,500- and 2,700-m contours are labelled. An array of 15 ocean-bottom receivers, 7 near- and 8 off-axis instruments (filled circles and squares, respectively), recorded data from over 400 explosive sources located within the inner box and from 90 shots located along two off-axis rise-parallel lines (small open circles). The inner box encompasses the region of previous crustal imaging, whereas the region of tomographic analysis of this study is shown by the outer box. The aperture of our experiment encompasses a 12-km-long linear rise segment, defined by two deviations from axial linearity ('devals') near 9° 28' N and 9° 35' N, and portions of adjacent segments to the north and south. Mantle refractions (P_n), observed as first-arrivals for source-receiver paths connecting the two lines located 20 km off-axis, sample structure within ~4 km of the Moho along a 30-km-long section of the rise. As the crustal legs of the P_n paths are positioned off-axis, this phase is not affected by the axial magma chamber and any delay-time anomaly is the result of variation in the structure of the off-axis crust or the uppermost mantle beneath the rise. Crustal phases constrain the structure of the upper 3 km of the crust beneath the source and receiver positions.

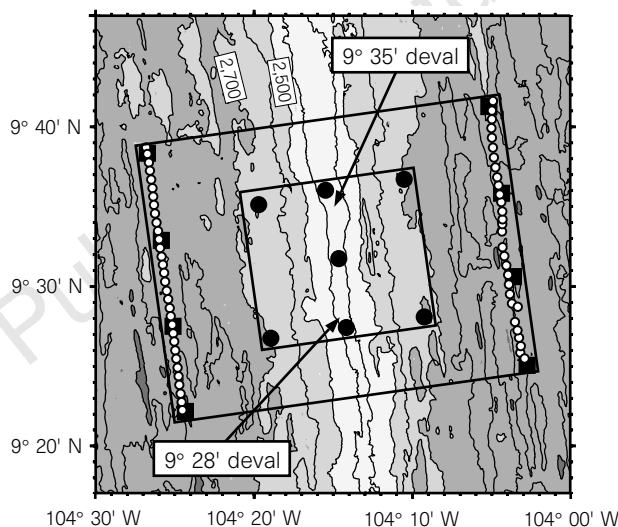
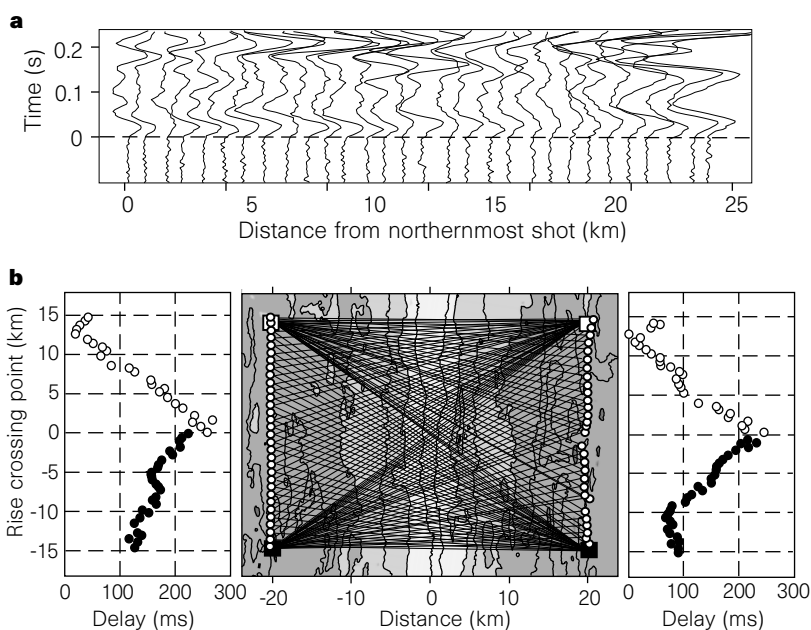


Figure 2 a, Record section showing seismograms from the westernmost sources as recorded by a receiver in the southeastern corner of the experiment (see Fig. 1). Traces are plotted by distance from the northernmost shot and are aligned at the P_n arrival; sampling interval is 4 ms. Source-receiver range along this line varies from 40 to 50 km; throughout this distance the signal-to-noise ratio and the trace-to-trace coherency are both good. P_n arrivals are identifiable to within 10–15 ms. Onset time and uncertainties are assigned by an automatic picking routine¹⁴. The r.m.s. uncertainty in the P_n data alone is 11 ms and the r.m.s. uncertainty in the P and P_n data combined with the experimental uncertainty (see ref. 14) is 9 ms. **b**, Travel-time delays, relative to a one-dimensional model, for four of the off-axis receivers and associated source-receiver pairs. Travel-time delays observed at the northernmost receivers (open circles) show a systematic increase of 250 ms towards the south. If this trend were entirely the result of variation in crustal structure near the source positions, then a matching signal would be predicted for a different pair of receivers recording the same sources. For a pair of receivers to the south (filled circles), such a signal is not observed, indicating that the source of the anomaly is located in the mantle. The delay-time anomaly is less for rise-perpendicular paths, a pattern consistent with seismic anisotropy when the fast axis is aligned with the spreading direction. Features indicative of axis-parallel heterogeneity are a delay-time signal that varies at several wavelengths and that, for rise-perpendicular paths, differs from north to south by 100 ms, with northern paths generally faster (smaller delay) than southern paths.



of anisotropy, were free to vary. The images of seismic heterogeneity are similar, particularly for models that include a component of anisotropy. For the results in Fig. 3, the final root-mean-squared (r.m.s.) residuals for the delay-time data were similar (~ 12 ms; a normalized variance reduction of 95% relative to the starting model). For the P_n data alone, a three-dimensional model achieves a 95% variance reduction (r.m.s. decreases from 87 to 44 ms), whereas the best-fitting two-dimensional model explains $<50\%$ of the data variance (r.m.s. decreases from 87 to 44 ms). The magnitude of seismic anisotropy is not well constrained, a result of the limited azimuthal sampling ($<40^\circ$) for a station that records P_n arrivals. A comparison of the images (Figs 3a–c) shows that anisotropy trades off primarily with the average upper-mantle velocity, with increasing anisotropy requiring a lower average velocity; an increase in percentage anisotropy results in faster propagation across the rise, whereas a lower average velocity has the opposite effect. We cannot choose a preferred model on the basis of data misfit alone. However, only models with 6–7% anisotropy (Fig. 3b or d) yield an average sub-axial P-wave velocity (7.3 km s^{-1}) consistent with the results of previous seismic refraction experiments^{10,11} performed in this area. Our preferred solutions (Fig. 3b and d) thus include a significant component of seismic anisotropy (6–7%) with the fast axis rotated $2\text{--}3^\circ$ anticlockwise with respect to the predicted spreading direction¹⁶.

We have performed a number of resolution tests to confirm that the P_n data require significant along-axis variation in sub-Moho structure. Synthetic tests (Fig. 3e–h) indicate that the available ray set reconstructs the approximate shape and magnitude of anomalous structures. Owing to the spatial smoothing operators,

however, the amplitude of a reconstructed anomaly trades off with its width such that the peak magnitude of a velocity perturbation may be underestimated by 15–20% (in terms of absolute velocity the difference is only $\sim 1\text{--}3\%$). Additionally, our results are effectively unchanged by expected variations in crustal thickness. A seismic-reflection study reports that the crustal thickness at the southern end of our experiment may be 1 km greater than at the northern end¹⁷. Such an increase in crustal thickness does not change the along-axis segmentation of the anomalous sub-Moho structure, though it does impart a linear gradient in velocity from north to south. Cross-axis variations in crustal thickness are minimal in this area^{8,17} and cannot explain the P_n delay-time anomaly. To quantify the vertical sensitivity of the P_n data, inversions were conducted for starting models similar to that in Fig. 3b and d, except that the deeper portions of the sub-axial anomaly were selectively removed. Several such inversions reconstructed the lowermost portions of the anomaly, confirming that the P_n data require a low-velocity region that is at least 4 km thick. This result is in agreement with the Fresnel zone of P_n arrivals, which at mantle depths are averaging structure within 2 km of the infinite-frequency ray path. We conclude that the tomographic image recovers along-axis variations in bulk properties averaged over the upper 4 km of the mantle.

A perspective view of the preferred model, along with the sea-floor relief, is shown in Fig. 4. The most prominent feature is the axially continuous region of anomalously low velocities. Directly beneath the rise axis the P-wave velocity, relative to off-axis upper-mantle velocities, is reduced by up to 12% near the experiment's centre and varies along-axis by 6–8% over distances of a few

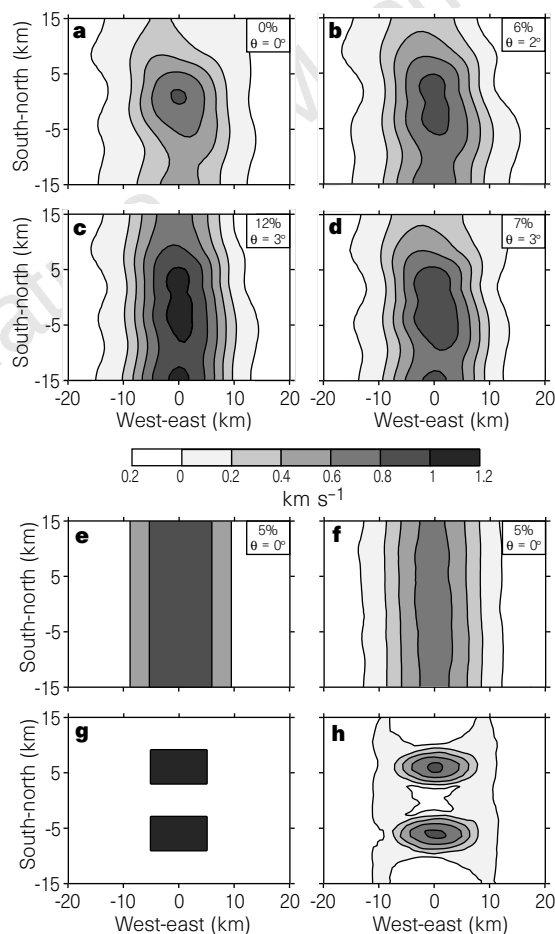


Figure 3 a–d. Results of tomographic analyses for different assumptions of seismic anisotropy. Map-view sections are taken at 8 km depth beneath the sea floor; images between 7 and 10 km depth are similar. Perturbations are shown relative to 8.2 km s^{-1} ; the grey scale changes at intervals of 0.2 km s^{-1} , from 0.0 to -1.2 km s^{-1} . The percentage anisotropy and orientation of the fast direction, with respect to the x-axis, are indicated in the box at the top right of a panel. The area of the sections corresponds to the outer box in Fig. 1; the y-axis is aligned with the regional trend of the EPR. For **a–c**, the magnitude of the anisotropy was fixed at 0%, 6% and 12%, respectively, and the tomographic analysis determined the direction of anisotropy and isotropic component of velocity. **d**, Results when all parameters (magnitude and orientation of anisotropy and isotropic component of velocity), were allowed to vary. For ray tracing, the seismic velocity model was parametrized within a $42 \times 31 \times 11 \text{ km}^3$ volume at intervals of 250 m and 200 m in the horizontal and vertical directions, respectively. In comparison with models where analytical solutions are available, this parametrization yields a standard deviation of 3 ms in the estimate of a P_n travel time (for all ranges and azimuths); further improvements in the accuracy of ray tracing do not affect the results of tomographic imaging. Our inversion method uses separately defined perturbational models for the isotropic velocity and anisotropy parameters. The perturbational model of isotropic velocity is defined at 1-km intervals in the horizontal directions and 0.5-km intervals in the vertical direction, except in the upper 3 km of the model where the vertical spacing is 0.2 km. The depth-dependent perturbational model for anisotropic parameters is defined within the Moho transition zone and the uppermost mantle at 1-km intervals. **e–h**, Tests of resolution. Synthetic travel-time data for two- and three-dimensional structures (**e** and **g**) were inverted using the procedure applied to actual data; random noise (zero mean, 10-ms standard deviation) was added to the data. The two-dimensional test model, **e**, includes an axis-parallel, low-velocity region and 5% seismic anisotropy. The reconstruction, **f**, demonstrates that the ray set does not introduce any significant three-dimensional structure. The three-dimensional synthetic model, **g**, includes two regions of anomalously slow velocities. The lateral velocity contrast of 1 km s^{-1} results in significant diffraction of energy around the anomalies and thus an underestimate of their spatial dimensions (**h**). However, the location, approximate dimensions, and peak amplitude of the low-velocity perturbations are recovered.

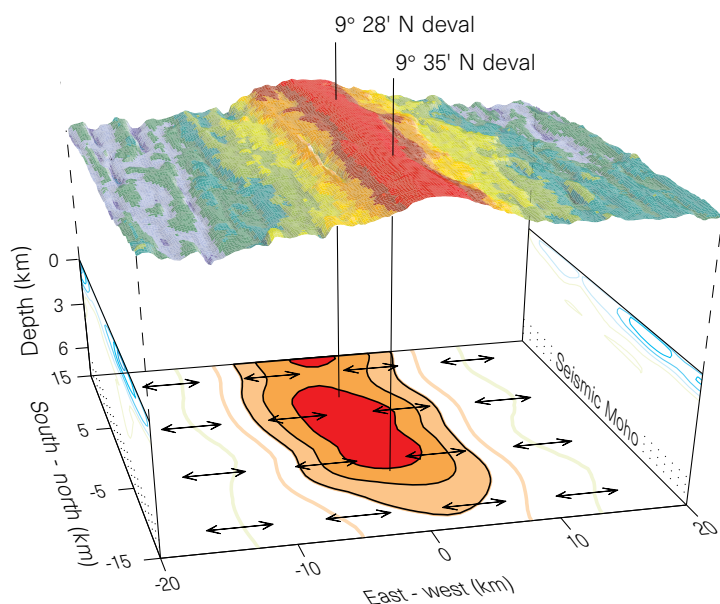


Figure 4 Sea-floor bathymetry and results of tomographic imaging shown in perspective view; solution is that of Fig. 3d. Perturbations in seismic velocity are shown relative to a one-dimensional model¹⁰ (8.2 km s^{-1} in the mantle) and contoured at intervals of 0.2 km s^{-1} . The vertical sections are located $\pm 20 \text{ km}$ from the rise axis; the horizontal section is at 8 km depth beneath the sea floor. The fast axis for the azimuthal P-wave anisotropy is depicted by the arrows. Vertical exaggeration of the bathymetry is five times and the locations of devals are shown by vertical lines. In the horizontal section, the filled areas represent the region predicted to contain $>1\%$ melt. The magnitude of the upper-mantle anomaly varies along-axis by more than a factor of 2 and the anomaly is clearly segmented, with the greatest perturbation (-1.0 km s^{-1}) located between the $9^\circ 28' \text{ N}$ and $9^\circ 35' \text{ N}$ devals. The upper-mantle anomaly lessens significantly in magnitude northward of the $9^\circ 35' \text{ N}$ deval and as far as the edge of our experiment aperture. This portion of the anomaly underlies a section of the rise that shows no evidence of active hydrothermal venting¹² and exhibits an AMC reflector that is about half the width of that to the south of the $9^\circ 35' \text{ N}$ deval⁹. Near the $9^\circ 28' \text{ N}$ deval, the anomaly again decreases in magnitude, before increasing towards the southern limit of the image. These along-axis variations in the magnitude of the upper-mantle anomaly have a striking correlation with the segmentation of sea-floor morphology^{2,5,12} and previously reported crustal images^{6,14}.

kilometres (down to 4% north of the $9^\circ 35' \text{ N}$ deval). The average cross-axis width of the anomaly ($\Delta v_p < -0.2 \text{ km s}^{-1}$, where v_p is P-wave velocity), nearly 18 km , is more than twice the width of the low-velocity volume observed in the crust (see Fig. 3 in ref. 6).

It is reasonable to assume that, at mantle depths, anomalously low seismic velocities are due to elevated temperatures and the presence of partial melt. As our experiment was removed from offsets in the rise that could influence the mantle thermal structure, the observed rise-parallel heterogeneity in seismic velocity is consistent with a region of partial melt that is variable along axis. Estimates of the absolute melt fraction depend on the cross-axis thermal structure. Within 10 km of the rise, thermal models^{18,19} predict maximum sub-Moho temperature differences of $<200^\circ \text{C}$, corresponding to a cross-axis velocity reduction of $<1\text{--}4\%$ (1% , ref. 20; 4% , ref. 21). Given these values, our results are compatible with a region of partial melt that is axially continuous. For film-like inclusions (aspect ratios of $0.1\text{--}0.01$), the range in melt fraction would be $1\text{--}5\%$; this range would double if melt is stored along grain boundary triple junctions^{22,23}. These estimates represent an average on the scale of the seismic wavelength and are in general agreement with values inferred from potential field data (see, for example, refs 24, 25).

The tomographic images of velocity structure at $9^\circ 30' \text{ N}$ (Fig. 4 and refs 6, 11, 14) indicate that mantle and crustal magmatic processes are segmented on a similar length scale. We suggest that the rise between the $9^\circ 28' \text{ N}$ and $9^\circ 35' \text{ N}$ devals overlies mantle that is at present delivering greater amounts of melt to sub-crustal and crustal reservoirs. As volcanic and hydrothermal processes are strongly linked to magmatic processes, we interpret the observed segmentation in crustal structure^{6,11,14}, axial morphology^{2,5,12}, and the spatial distribution of hydrothermal vent fields¹² as a consequence of focused ascent of magma at mantle depths. For a section of the EPR bounded by tectonic offsets, such as transform faults or overlapping spreading centres, several regions of enhanced melt supply from the mantle to the crust are predicted to exist along-axis. □

Received 13 March; accepted 27 May 1997.

1. Parmentier, E. M. & Phipps Morgan, J. Spreading rate dependence of three-dimensional structure in oceanic spreading centres. *Nature* **348**, 325–328 (1990).
2. Macdonald, K. C. *et al.* A new view of the mid-ocean ridge from the behaviour of ridge-axis discontinuities. *Nature* **335**, 217–225 (1988).

3. Bell, R. E. & Buck, W. R. Crustal control of ridge segmentation inferred from observations of the Reykjanes Ridge. *Nature* **357**, 583–586 (1992).
4. Nicolas, A., Boudier, F. & Ildefonse, B. Evidence from the Oman ophiolite for active mantle upwelling beneath a fast-spreading ridge. *Nature* **370**, 51–53 (1994).
5. Langmuir, C. H., Bender, J. F. & Batiza, R. Petrological and tectonic segmentation of the East Pacific Rise, $5^\circ 30' \text{--}14^\circ 30' \text{ N}$. *Nature* **322**, 422–429 (1986).
6. Toomey, D. R., Purdy, G. M., Solomon, S. C. & Wilcock, W. S. D. The three-dimensional seismic velocity structure of the East Pacific Rise near latitude $9^\circ 30' \text{ N}$. *Nature* **347**, 639–645 (1990).
7. Sinton, J. M. & Detrick, R. S. Mid-ocean ridge magma chambers. *J. Geophys. Res.* **97**, 197–216 (1992).
8. Detrick, R. S. *et al.* Multi-channel seismic imaging of a crustal magma chamber along the East Pacific Rise. *Nature* **326**, 35–41 (1987).
9. Kent, G. M., Harding, A. J. & Orcutt, J. A. Distribution of magma beneath the East Pacific Rise between the Clipperton transform and the $9^\circ 17' \text{ N}$ Deval from forward modeling of common depth point data. *J. Geophys. Res.* **98**, 13945–13969 (1993).
10. Vera, E. E. *et al.* The structure of 0- to 0.2-m.y.-old oceanic crust at 9° N on the East Pacific Rise from expanded spread profiles. *J. Geophys. Res.* **95**, 15529–15556 (1990).
11. Wilcock, W. S. D., Solomon, S. C., Purdy, G. M. & Toomey, D. R. Seismic attenuation structure of the East Pacific Rise near $9^\circ 30' \text{ N}$. *J. Geophys. Res.* **100**, 24147–24165 (1995).
12. Haymon, R. M. *et al.* Hydrothermal vent distribution along the East Pacific Rise crest ($9^\circ 09' \text{--}54' \text{ N}$) and its relationship to magmatic and tectonic processes on fast-spreading mid-ocean ridges. *Earth Planet. Sci. Lett.* **104**, 513–534 (1991).
13. Reynolds, J. R., Langmuir, C. H., Bender, J. F., Kastens, K. A. & Ryan, W. B. F. Spatial and temporal variability in the geochemistry of basalts from the East Pacific Rise. *Nature* **359**, 493–499 (1992).
14. Toomey, D. R., Solomon, S. C. & Purdy, G. M. Tomographic imaging of the shallow crustal structure of the East Pacific Rise at $9^\circ 30' \text{ N}$. *J. Geophys. Res.* **99**, 24135–24157 (1994).
15. Babuska, V. & Cara, M. *Seismic Anisotropy in the Earth 1–217* (Kluwer Academic, Boston, 1991).
16. DeMets, C., Gordon, R. G., Argus, D. F. & Stein, S. Current plate motions. *Geophys. J. Int.* **101**, 425–478 (1990).
17. Barth, G. A. & Mutter, J. C. Variability in oceanic crustal thickness and structure: Multichannel seismic reflection results from the northern East Pacific Rise. *J. Geophys. Res.* **101**, 17951–17975 (1996).
18. Phipps Morgan, J. & Chen, Y. J. The genesis of oceanic crust: Magma injection, hydrothermal circulation, and crustal flow. *J. Geophys. Res.* **98**, 6283–6298 (1993).
19. Henstock, T. J., Woods, A. W. & White, R. S. The accretion of oceanic crust by episodic sill intrusion. *J. Geophys. Res.* **98**, 4143–4161 (1993).
20. Humphreys, E. D. & Dueker, K. G. Physical state of the western U.S. upper mantle. *J. Geophys. Res.* **99**, 9635–9650 (1994).
21. Karato, S. Importance of anelasticity in the interpretation of seismic tomography. *Geophys. Res. Lett.* **20**, 1623–1626 (1993).
22. Schmeling, H. Numerical models on the influence of partial melt on elastic, anelastic and electric properties of rocks. Part I: Elasticity and anelasticity. *Phys. Earth Planet. Inter.* **41**, 34–57 (1985).
23. Faul, U. H., Toomey, D. R. & Waff, H. S. Intergranular basaltic melt is distributed in thin, elongated inclusions. *Geophys. Res. Lett.* **21**, 29–32 (1994).
24. Madsen, J. A., Forsyth, D. W. & Detrick, R. S. A new isostatic model for the East Pacific Rise crest. *J. Geophys. Res.* **89**, 9997–10015 (1984).
25. Wang, X., Cochran, J. R. & Barth, G. Gravity anomalies, crustal thickness, and the pattern of mantle flow at the fast spreading East Pacific Rise, $9^\circ\text{--}10^\circ \text{ N}$: Evidence for three-dimensional upwelling. *J. Geophys. Res.* **101**, 17927–17940 (1996).

Acknowledgements. We thank the officers and crew of the RV *Thomas Washington* and members of the scientific party for their assistance; A. Barclay, R. Detrick, R. Evans, E. Humphreys, Y. Shen, W. Wilcock and C. Wolfe for discussions and reviews of the manuscript; and C. Harrop and the Computational Science Institute at the University of Oregon for their assistance and resources. This work was supported by the NSF, the Office of Naval Research, and a University of Oregon doctoral fellowship.

Correspondence should be addressed to R.D. (e-mail: rob@newberry.uoregon.edu).